Simulations of microlayer formation in nucleate boiling

Alexandre Guion[1], Shahriar Afkhami[2], Stephane Zaleski [3], and Jacopo Buongiorno [1]†

[1]Department of Nuclear Science and Engineering, Massachusetts Institute of Technology, Cambridge, MA, USA

[2]Department of Mathematical Sciences, New Jersey Institute of Technology, Newark, NJ, USA

[3]Sorbonne Universités, UPMC Univ Paris 06, CNRS, UMR 7190, Institut Jean le Rond d'Alembert, F-75005, Paris, France

(Received xx; revised xx; accepted xx)

As a bubble grows outside of a cavity during nucleate boiling, viscous effects can be large enough compared to surface tension to impede liquid motion and trap a thin liquid layer, referred to as liquid microlayer, underneath the growing bubble. In practice, numerical simulations of nucleate boiling resolve the macroscopic liquid-vapor interface of the bubble, but resort to subgrid models to account for micro scale effects, such as the evaporation of the liquid microlayer. Evaporation models require initialization of the microlayer shape and extension, but models for microlayer formation are either physically incomplete or purely empirical. In this work, the Volume-Of-Fluid (VOF) method, implemented in the Gerris code, is used to numerically reproduce the hydrodynamics of hemispherical bubble growth at a wall, and resolve the formation of the liquid microlayer with an unprecedented resolution. Simulations are validated against the latest experimental data and compared to existing analytical models. Lastly, remaining gaps in building a generally applicable model for the formation of the microlayer are presented.

Key words: Authors should not enter keywords on the manuscript, as these must be chosen by the author during the online submission process and will then be added during the typesetting process (see http://journals.cambridge.org/data/relatedlink/jfm-keywords.pdf for the full list)

1. Introduction and motivation

The transport of latent heat makes boiling one of the most efficient mode of heat transfer, allowing a wide range of systems to improve their thermal performance, from nuclear power plants to microelectronic devices - see reviews by Yeh (1995), Manglik (2006), and Kandlikar (2012). Subcooled boiling heat transfer for example is able to accommodate very high heat fluxes, thus cooling components very efficiently.

Predicting boiling heat transfer has therefore garnered significant attention, but remains complicated by the need to consider phenomena occurring over multiple scales - see Figure 1, from the adsorbed liquid layer at the wall at the nanometer scale - see Churaev (1975) and Chung *et al.* (2011), up to the bubble diameter at the millimeter scale, see Dhir (1998), Stephan & Kern (2004), Kim (2009), Kunkelmann & Stephan

† Email address for correspondence: jacopo@mit.edu

(2010), Guion *et al.* (2013), Jiang *et al.* (2013), Jung & Kim (2014), Sato & Niceno (2015), Giustini *et al.* (2016), Zou *et al.* (2016*a*), and Zou *et al.* (2016*b*).

1.1. *Physical phenomena*

During nucleate boiling a bubble grows outside of a surface imperfection, referred to as cavity, and from a preexisting embryo of vapor initially trapped in that surface imperfection. Boiling starts at the wall when the local temperature is sufficiently high to allow the vapor bubble to exist and grow outside of the cavity and into the surrounding liquid, see Bankoff (1958).

At the inception of nucleate boiling at a cavity, the liquid in the vicinity of the heated wall is superheated and mass transfer occurs at the liquid-vapor interface of the bubble. The growth of the bubble is also fueled by the overpressure within the vapor, and impeded by the inertia of the liquid. During this initial phase of rapid growth, often referred to as the inertia-controlled phase of bubble growth, the bubble grows hemispherically, see Figure 2: bubble growth rates, U_b, based on bubble cross section area, bubble height, and bubble width are identical.

We define a capillary number Ca associated with bubble growth rate as:

$$Ca = \mu_l U_b / \sigma$$

with μ_l the liquid viscosity and σ the surface tension coefficient. As the bubble grows outside of the cavity, Ca can be large enough to impede liquid motion at the wall and trap a thin liquid layer underneath the bubble: the liquid microlayer - see experimental evidence by Moore & Mesler (1961), Hendricks & Sharp (1964), Hospeti & Mesler (1965), Jawurek (1969), Foltz & Mesler (1970), Judd (1975), Judd & Hwang (1976), Koffman & Plesset (1983), Moghaddam & Kiger (2009), Golobic *et al.* (2009), Kim & Buongiorno (2011), Gao *et al.* (2013), Jung & Kim (2014), Jung & Kim (2015), Bigham & Moghaddam (2015), Yabuki & Nakabeppu (2014), Yabuki & Nakabeppu (2016), and Zou *et al.* (2016*a*).

Once the bubble has reached a certain size, referred to as departure diameter, the bubble departs from its initial position at the heated wall and additional cooling mechanisms can occur.

From measurements of microlayer thickness over time by Kim & Buongiorno (2011) in the case of water at atmospheric pressure, we identify two separate time scales τ_1 and τ_2 representative of microlayer formation and evaporation, respectively: $\tau_1 \sim 10 - 100\mu s$, and $\tau_2 \sim 1 - 10ms$. Hemispherical bubble growth was observed at both time scales - see Figure 2.

1.2. *Modeling of boiling heat transfer*

In the past, various empirical correlations and mechanistic models have been proposed to describe and predict boiling heat transfer - see reviews by Dhir (1998), Manglik (2006), and Warrier & Dhir (2006). A wide range of boiling surface geometries, materials, working fluids, and operating conditions have been investigated. In particular, heat partitioning models by Judd & Hwang (1976), Kurul & Podowski (1990), and Gilman (2014) provide a mechanistic description of the wall boiling phenomena: the total heat flux at the wall is divided into separate heat flux components that account for various modes of heat transfer at the wall, such as forced convection, evaporation, quenching, and sliding conduction. In this context, recent advanced diagnostics (Infrared Imagery, Particle Image Velocimetry, High Speed Video Imagery, and etc.) provide new and highly-resolved experimental data that can inform and validate models or correlations describing

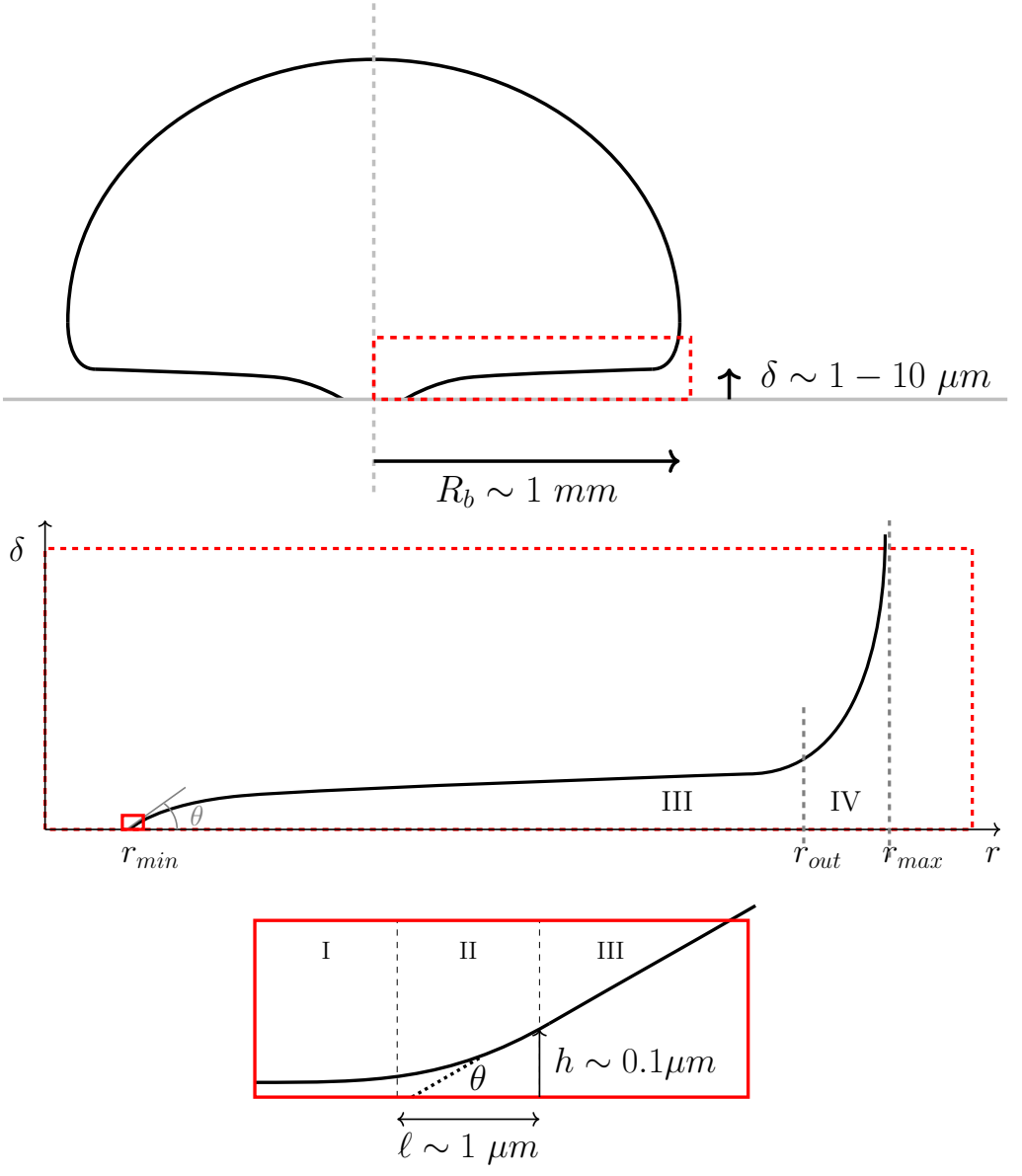

Figure 1: Multiple scales involved in nucleate boiling: from the millimeter scale at the bubble cap (top) to the nanometer scale at the adsorbed liquid layer (Region I, right insert). Region I: adsorbed layer region of thickness $h_0 \sim 1 - 10nm$. Region II: transition region between the non-evaporating adsorbed layer and the evaporating liquid microlayer ($h \geqslant h_0$ and $h \lesssim 100nm$). Region III: central microlayer region of typical thickness $\delta \sim 1 - 10\mu m$. Note in the insert the black dotted line that represents the Triple Phase Line (TPL) where the three phases (liquid, vapor, and solid) are in apparent contact. The contact angle θ represents the angle between the contact line and the substrate at the microscopic scale. Region IV: microlayer outer-edge region of typical thickness $\delta \geqslant 10\mu m$, where the thickness rapidly increases from the central region to the bubble cap.

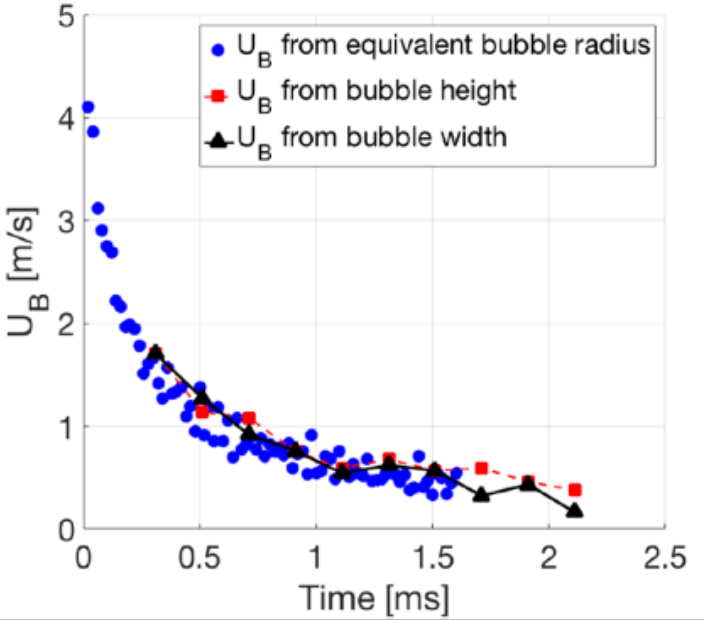

Figure 2: Bubble growth rate U_b as a function of time based on bubble cross section area, bubble height, and bubble width recorded by a High Speed Video camera on the side of the growing bubble (Courtesy of Prof. Hyungdae Kim). Fluid is water at saturation and atmospheric pressure. Typical time scales $\tau_1 \sim 10 - 100\mu s$, and $\tau_2 \sim 1 - 10ms$ are representative of microlayer formation and evaporation, respectively. Hemispherical bubble growth was observed at both time scales.

each individual component of the wall heat flux, as they individually represent a single specific physical phenomenon at the wall - see the review by Buongiorno *et al.* (2014). Through careful calibration and post-processing, it is possible to accurately measure the temperature and heat flux distributions on the boiling surface which reveals detailed features, including the effects of evaporation of the liquid microlayer as shown by Gerardi (2009) and Kim (2009). Depending on the fluid, flow and nucleation temperature, the contribution from microlayer evaporation to overall heat transfer and bubble growth can be large in the case of water, see Gerardi (2009), or relatively small in the case of refrigerants, see Kim (2009). Typical microlayer models focus on evaporation at the Triple-Phase-Line (TPL) region where the three phases (liquid, solid, and vapor) are in apparent contact, see Dhir (2009) and Kunkelmann & Stephan (2010), or in the extended microlayer region, see Guion *et al.* (2013), Jiang *et al.* (2013), and Sato & Niceno (2015). In practice, numerical simulations of boiling resolve the macroscopic liquid vapor interface of boiling bubbles, but typically resort to subgrid models to include contributions at the microscopic scale such as from evaporation of the microlayer, which requires initialization of the microlayer shape and extension.

1.3. *Current gaps and proposed strategy*

Existing models of microlayer formation are either physically incomplete, e.g. do not include the effect of surface tension or contact angle, see Van Stralen *et al.* (1975), or are purely empirical, see Sato & Niceno (2015). The objective of the present work is to leverage existing numerical methods to build a large numerical database and

inform mirolayer formation, clarify remaining modeling challenges, and eventually build a generally applicable model for the formation of the microlayer. Existing experimental data that directly measures microlayer thickness profiles, see work from Judd (1975), Koffman & Plesset (1983), Kim & Buongiorno (2011), Jung & Kim (2014), and Jung & Kim (2015), does not cover a wide range of fluids and surfaces, which makes it difficult to generate or validate a general model on microlayer formation. In practice, measurements of microlayer thickness profiles are mostly obtained at times where the microlayer has already started to evaporate, with little insight on its formation dynamics. Recent advances by Yabuki & Nakabeppu (2016) in indirect measurements of microlayer thickness at short time scales can offer new insights and will be discussed.
In the present work, we use Computational Fluid Dynamics with Interface Tracking Methods to numerically reproduce the hydrodynamics of bubble growth at a wall, and resolve the formation of the liquid microlayer at the wall for a wide range of conditions and fluids. For all simulated cases, the Volume-Of-Fluid Method implemented in the Gerris flow solver from Popinet (2009) is used to accurately track the liquid vapor interface over time, and predict the formation of the microlayer.

1.4. *Assumptions made in this work*

In this work, we focus on the mechanisms of microlayer formation. In particular, we only consider the hydrodynamics of bubble growth at the wall, and neglect thermal effects, separating microlayer formation ($\tau_1 \sim 10 - 100\mu s$) from microlayer evaporation ($\tau_2 \sim 1 - 10ms \gg \tau_1$). Part of the liquid layer that forms at the wall may also evaporate during such short time scales τ_1, hence affecting its shape over time. However, we estimate that only 10% or less of the thickness of the liquid microlayer would be affected by evaporation during the formation phase, for a typical wall superheat at the wall ΔT ($\Delta T = 1$ to $10K$) observed experimentally at atmospheric pressure, and considering evaporation from pure conduction through the liquid layer, for various growth times (1 to $100\mu s$), and various layer thicknesses (0.1 to $10\mu m$). Thermal effects, including the effect of mass transfer, on the motion of the contact line at short time scales are not included in the scope of the present work. Long range interaction forces of the liquid film with the substrate are also neglected as they may be relevant only at very short time scales where the film is very thin - see for example Rednikov & Colinet (2013). In this work, we implement a static contact angle at a wall for simplicity, which allows the contact line to move. However, one could replace it with a specific mobility law that would describe the behavior of the microscopic contact angle in the conditions of interest. Mesh dependence of moving contact lines simulations with grid size as previously shown by Moriarty & Schwartz (1992), Weinstein & Pismen (2008), and Afkhami *et al.* (2009) is reported elsewhere, see Afkhami *et al.* (2017).

1.5. *Contributions and structure of the paper*

This work focuses on three main contributions: (i) identify the minimum set of dimensionless parameters that controls the hydrodynamics of microlayer formation at a wall during nucleate pool boiling (ii) generate a numerical database that resolves the dynamics of microlayer formation for all conditions of interest (e.g. water in lab experiment at atmospheric pressure, water at nuclear reactor pressure conditions), and (iii) identify remaining gaps in building a generally applicable model for microlayer formation, to be used during the initialization of boiling simulations. This paper specifically focuses on the central microlayer region, see region III in Figure 1. Future work includes modeling the outer-edge region, see region IV in Figure 1, using the present numerical database,

and modeling the particular contact line dynamics using experimental data for specific wall conditions and for the fluid/solid pair of interest.

In section 2 we provide a dimensional analysis and general functional dependence for the microlayer formation dynamics. In section 3 we describe the computational framework used to simulate microlayer formation, and verify the correct implementation and convergence of the methods used. In section 4 we discuss the reduction of the parameter space, qualitative trends, and numerical results used to model microlayer formation, in particular we compare our results in the central region (region III, Figure 1) with the analytical model from Cooper & Lloyd (1969) and with latest experimental results measuring microlayer thickness at early times. In section 5 we conclude by discussing the contributions of this present work and the remaining opportunities for future work.

2. Problem statement and dimensional analysis

We consider the early growth of a steam bubble near the wall of a pool of initially stagnant liquid. We take advantage of the symmetry of the growth and consider the problem to be axisymmetric. Ten physical variables are involved in describing the hydrodynamics of microlayer formation: liquid and vapor viscosities, μ_l and μ_v, respectively; liquid and vapor densities, ρ_l and ρ_v, respectively; surface tension, σ; bubble growth rate, U_b, the velocity at which the liquid/vapor interface moves inside the surrounding liquid; microscopic contact angle between the liquid vapor interface and the wall at a given reference length scale dx, the minimal mesh size, θ; radial distance from bubble root, r; time, t; and the unknown local thickness of the liquid microlayer forming at the wall, δ. Altogether, these ten variables involve three physical dimensions, and seven dimensionless Pi-groups can fully describe microlayer formation. The proposed dimensionless Pi-groups are:

$$\begin{aligned}
\Pi_1 &= \delta/r_c = \delta^* \\
\Pi_2 &= \mu_l/\mu_v = \mu^* \\
\Pi_3 &= \rho_l/\rho_v = \rho^* \\
\Pi_4 &= r/r_c = r^* \\
\Pi_5 &= t/t_c = t^* \\
\Pi_6 &= \theta \\
\Pi_7 &= Ca = \mu_l U_b/\sigma
\end{aligned}$$

where the reference length and time scales r_c and t_c were defined as follows:

$$r_c = \mu_l/(\rho_l U_b) \tag{2.1}$$

$$t_c = r_c/U_b = \mu_l/(\rho_l U_b^2) \tag{2.2}$$

with r_c based on Reynolds number $Re = 1$, for which inertia of the liquid surrounding the bubble and viscous forces at the wall would be comparable. A unique functional form describes the microlayer shape δ^* as a function of the six other Pi-groups, which can be written as follows:

$$\delta^* = f(\mu^*, \rho^*, r^*, t^*, Ca, \theta) \tag{2.3}$$

In this study we have performed numerical simulations of microlayer formation to quantify f (Eq. 2.3). The relevant parameter space for liquid water boiling in lab

and industrial conditions (Pressurized Water Reactors, or PWR) is as follows: $\mu_l/\mu_v \in [3.2;\ 23.3]$, $\rho_l/\rho_v \in [5.9;\ 1650]$, $Ca \in [0.001;\ 0.1]$, $\theta \in [0;\ 90°]$. The range of capillary number, Ca, is obtained from water properties at saturation (μ_l and σ) for both pressures (0.101MPa and 15.5MPa), and estimates of bubble growth rates U_b from Mikic *et al.* (1970), including a range of cavity mouth radius r_b:

$$U_b = \sqrt{\pi h_{fg} \rho_v \Delta T_{sat} / (7 \rho_l T_{sat})} \tag{2.4}$$

where ΔT_{sat} is the so-called wall superheat at the inception of boiling:

$$\Delta T_{sat} = 2\sigma T_{sat} / (r_b \rho_v h_{fg}) \tag{2.5}$$

with T_{sat} the saturation temperature, and h_{fg} the latent heat of vaporization. In practice, bubble growth rate U_b and wall superheat ΔT_{sat}, estimated using Eq. 2.4 and 2.5, are experimentally measured.

3. Computational framework

A myriad of methods are available today to simulate two phase flows while tracking the interface between two fluids - see recent review by Kharangate & Mudawar (2017). The Volume-Of-Fluid (VOF) method, see Scardovelli & Zaleski (1999), tracks the interface using a color function C that represents the volume fraction of one phase in each cell of the computational domain. Starting from an initial distribution, the color function C is then advected by the flow:

$$\partial C\rho/\partial t + \nabla.(C\rho\vec{U}) = S \tag{3.1}$$

The Gerris Flow Solver by Popinet (2009) (gfs.sourceforge.net/) solves the incompressible Navier-Stokes equations, and implements the VOF method to track the interface and compute the surface tension force:

$$\rho(\partial\vec{U}/\partial t + \vec{U}.\nabla\vec{U}) = -\nabla p + \nabla.(2\mu\bar{\bar{D}}) + \sigma\kappa\delta_s\vec{n} + \vec{F}_{external} \tag{3.2}$$

$$\partial\rho/\partial t + \nabla.(\rho\vec{U}) = S \tag{3.3}$$

$$\nabla.\vec{U} = S \tag{3.4}$$

where S is a volume source such that $\nabla.\vec{U} = S$; $\vec{U}$ is the velocity field; p is the pressure; κ is the curvature of the liquid vapor interface; $\vec{n}$ is the unit vector normal to the liquid vapor interface; $\bar{\bar{D}}$ is the rate of strain $\bar{\bar{D}} = \nabla U + (\nabla U)^T$; ρ is the fluid density, $\rho = C\rho_l + (1-C)\rho_v$; μ is the fluid viscosity, $\mu = C\mu_l + (1-C)\mu_v$.

The computational domain in Gerris is spatially discretized using a quad mesh, which allows refining specific regions in space while coarsening others. In this work, we typically refine in the vicinity of the wall and at the interface to resolve microlayer formation, while coarsening away from the wall and the bubble interface where such refinement is not necessary. We include a time-dependent volumetric source of vapor within the vapor phase to reproduce the growth observed in lab experiments. The source of vapor fuels bubble growth uniformly inside the bubble, and pushes the liquid vapor interface at the desired rate U_b, hence reproducing the hydrodynamics of hemispherical bubble growth. A time-dependence of the source is necessary to reproduce the sustained growth of the bubble as its volume increases. For a given constant bubble growth rate U_b ($U_b = dR_b/dt$) during the initial inertia-controlled phase of bubble growth, one can compute the volumetric

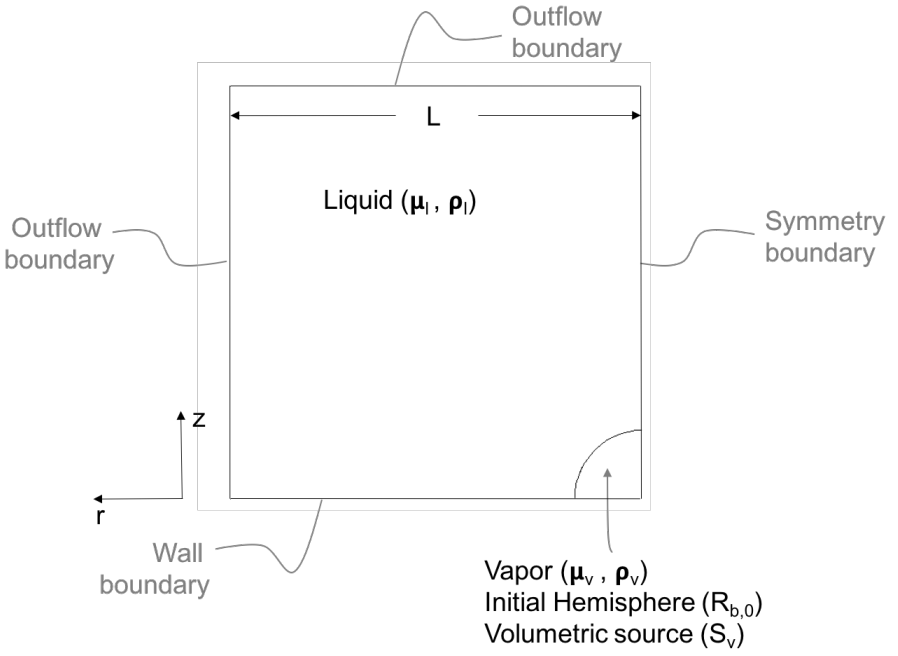

Figure 3: Computational domain for implementing a volumetric source of vapor to control the growth of the bubble in the presence of a wall.

growth rate dV_b/dt of the equivalent hemispherical bubble as follows:

$$dV_b/dt = 2\pi R_b^2 (dR_b/dt) = 2\pi R_b^2 U_b \tag{3.5}$$

The rate of change of the equivalent hemispherical bubble dV_b/dt is obtained by imposing a volumetric source term S in the vapor phase of volume V_b:

$$SV_b = dV_b/dt \tag{3.6}$$

Rearranging Eq. 3.6, we obtain an explicit expression for the volumetric source term S to impose in the vapor phase:

$$S = (dV_b/dt)/V_b = 3U_b/(R_{b,0} + U_b t) \tag{3.7}$$

Note the volumetric source term S is uniform in space within the vapor phase at all times, yet time dependent, and function of three parameters: the bubble growth rate U_b known from experiments or derived from Mikic's theory, see Mikic *et al.* (1970), the initial bubble radius $R_{b,0}$ prescribed during the initialization of the numerical simulation, and the physical time t. We typically simulate the growth of the bubble outside of the cavity, and initialize the bubble radius $R_{b,0}$ as the cavity mouth radius r_b (see Eq. **??**).

Method verification

We verify the implementation of the volumetric source term in axisymmetric configuration in Gerris in the absence of a wall, for the special case of a spherical bubble growth in a (semi)-infinite medium. We compare the volume and shape of the bubble to its simple analytical and spherical reference, and confirm convergence with grid size.

We also verify the convergence of the proposed method in the presence of a wall - see Figure 3. Two figures of merit are considered: the shape of the liquid microlayer

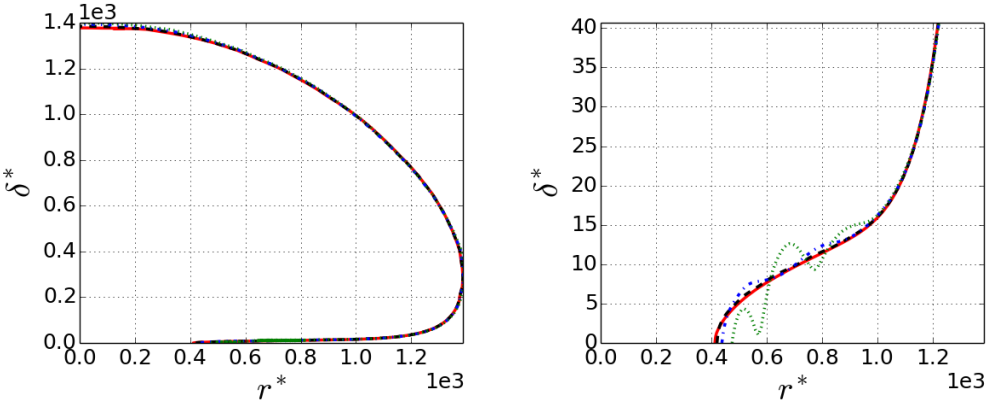

(a) (b)

Figure 4: Axisymmetric shapes of the macroscopic bubble (a) and liquid microlayer (b) obtained in four simulations of bubble growth at a wall, with increased refinement $\mathrm{dx}^* \in \{1, 1/2, 1/4, 1/8\}$ in the band: $0 \leqslant \delta^* \leqslant 160$ at the wall, while the refinement elsewhere at the interface is kept identical: $\mathrm{dx}^* = 4$, with $R^*_{b,0} = 40$ and $r_c = 0.025$ μm.

forming at the wall, and the macroscopic bubble growth rate obtained from imposing the volumetric source of vapor inside the bubble. Four simulations of bubble growth at a wall are reported here, with increased refinement in the microlayer region: $\mathrm{dx}/R_{b,0}$= 1/40, 1/80, 1/160, 1/320 ($R_{b,0} = 10\mu m$), specifically in a band of thickness $0.4R_{b,0}$ at the wall. Refinement elsewhere at the interface is kept identical: $\mathrm{dx}/R_{b,0}$=1/10. All four simulations yield identical macroscopic bubbles shapes - see Figure 4(a). In Figure 4(b), the microlayer shape converges to a single profile as we refine the mesh in the microlayer region, from $\mathrm{dx} = 250$ nm down to 125 nm, 62.5 nm, and 31.25 nm.

4. Numerical simulation results

Four regions (and scales) can be identified based on the curvature of the bubble interface, see Figure 5: (i) the contact line region where the interface meets the wall (negative curvature), (ii) the central region of the liquid microlayer ($\approx$ zero curvature), (iii) the microlayer outer-edge region that connects the central region with the macroscopic bubble cap (up to the bubble nose where the curvature peaks), (iv) the macroscopic hemispherical bubble cap (uniform curvature along the interface).

4.1. *Reducing the parameter space*

We perform simulations with all four bounding values for both viscosity and density ratios, and we note the weak dependence of the microlayer shape within both ranges of interest. This weak dependance is supported by the argument that the properties of the liquid phase affect the hydrodynamics of this problem much more than those of the vapor phase, which in practice can be considered as an inviscid and massless fluid. Therefore, in the rest of the study, we will no longer consider the dependence of the microlayer formation on the viscosity and density ratios, which simplifies the function in Eq 2.3 for the conditions of interest.

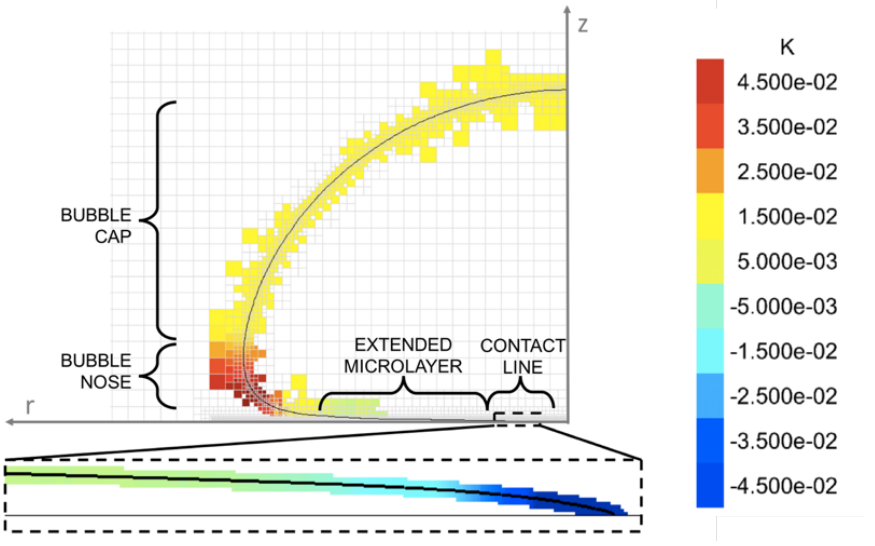

Figure 5: Typical axisymmetric shape of a growing bubble at a wall. Interface is solid black line. Curvature κ is given by the colormap: blue in the contact line region is negative curvature (minimum reached at the contact point $\kappa = -6.6\ 10^{-1}$ $[1/\mu m]$), green in the central linear region is approaching zero curvature ($\kappa \approx 10^{-3}$ $[1/\mu m]$), red at the bubble nose is maximum curvature ($\kappa = 5.8\ 10^{-2}$ $[1/\mu m]$), and yellow is the uniform curvature along the interface at the bubble cap as the bubble grows hemispherically ($\kappa \approx 1.5\ 10^{-2}$ $[1/\mu m]$). The range used in the color map does not reflect the maximum positive value and minimum negative value taken by the curvature, but rather is centered around 0 to allow easier identification of all four regions, also denoted in the image with direct labeling.

4.2. *Modeling the microlayer inner edge*

A general model of moving contact lines is out of the scope for the present paper. However, we identify multiple scenarios that could take place at the inner edge of the microlayer, where the liquid/vapor interface meets the solid surface: i) no motion of the contact line, pinned either at the cavity mouth or elsewhere on the wall surface, ii) intermittent motion of the contact line, where pinning and depinning of the contact line occurs at the wall, and iii) continuous motion of the contact line, that could be described by a mobility law $\theta = g(Ca_{cl})$, with Ca_{cl} the capillary number associated with the motion of the contact line, and θ the contact angle. When the contact line is free to move (no pinning), its motion relative to the bubble growth dictates whether a microlayer forms at the wall or not.

Qualitatively, the radial component of the surface tension force applied to a liquid wedge decreases in magnitude for increasing contact angles. Hence the contact line is expected to move faster at higher contact angles and the wetted fraction underneath the bubble is expected to be reduced at higher contact angles. Quantitatively, physical models or experimental data on contact line motion are needed to conclude on whether a microlayer is expected to form or not, for a given fluid/solid pair and surface condition, which cannot be resolved by the Gerris flow solver alone. In this work, we simulate moving contact lines for a wide range of constant and uniform contact angles at the wall, ranging from 20° to 90°. An extension of this work could include a physical mobility law to apply

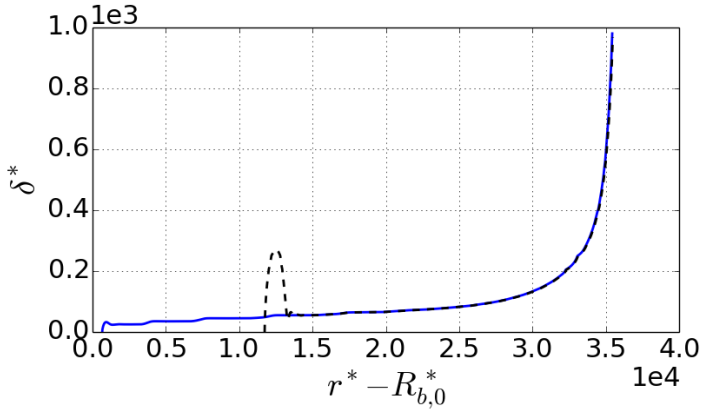

Figure 6: Microlayer thickness profiles δ^* for two contact angles $\theta = 20°$ (blue solid line) and $\theta = 80°$ (black dashed line), as a function of dimensionless radial distance $r^* - R^*_{b,0}$. Ca=0.1, $t^* = 3.6\ 10^3$ ($r_c = 10nm$, $t_c = 1ns$).

the proposed methodology to a specific application for which the physical motion of the contact line is known.

The simulation of moving contact lines is made possible with Gerris through the use of a height-function based model of contact angle implemented by Afkhami & Bussmann (2008), where a numerical contact angle θ is imposed in the cell at the wall containing the contact line. This microscopic contact angle is used to define the normal to the interface at the contact line, and therefore impacts both the computed curvature and the resulting surface tension force at the contact line. Cell normal velocities are used to advect volume fractions, resulting in an implicit slip along no-slip boundaries such as along the wall, which allows the contact line to move at the wall with the prescribed microscopic contact angle θ. As a consequence, the dynamics of the simulated moving contact line depend both on the microscopic contact angle prescribed and on grid size. Specific mesh convergence studies are reported in other papers, including most recently in Afkhami *et al.* (2017).

Typical simulation results are shown in Figure 6: we confirm that the wetted fraction underneath the bubble is reduced for higher contact angles, and we note the formation of a bulge of liquid at the inner edge of the microlayer. The surface tension force acts at the inner edge against the viscous force at the wall and pushes the contact line outwards, similar to the classic hole expansion problem, see Taylor & Michael (1973), Brenner & Gueyffier (1999), Savva & Bush (2009), Gordillo *et al.* (2011), and Agbaglah *et al.* (2013). The Ohnesorge number Oh is defined as:

$$Oh = \mu_l / \sqrt{\delta \rho_l \sigma} = \sqrt{Ca/\delta^*}$$

Three regimes are identified based on the Ohnesorge number: $Oh < 0.1$, $Oh \in [0.1; 10]$, and $Oh > 10$. As Oh increases, the capillary waves found at the tip disappear through the action of viscosity. In all simulations presented in this paper, we find that Oh ranges from $0.001 to 0.1$, which corresponds to the first regime where capillary waves are expected in the vicinity of the tip, and damped away from the tip due to viscous effects, leaving the rest of the extended liquid layer unaffected by the motion of the rim, as confirmed in Figure 6.

The microscopic contact angle θ used in Gerris allows us to represent the behavior of

the moving contact line as a boundary condition, or subgrid model, without attempting to resolve the complex physics at play at the scale of the contact line. For simplicity in the rest of the paper, we present results for low microscopic contact angles in order to observe microlayer formation. However, the informed reader would need to consider the specific motion of the contact line for the wall condition and solid/fluid pair of interest in order to determine whether a microlayer forms or not in such conditions, and quantify the relative motion of the contact line with respect to the macroscopic bubble.

4.3. *Modeling the microlayer central region*

An analytical model for microlayer formation has been proposed by Cooper & Lloyd (1969), using a simplified, single-phase boundary layer description of the two phase flow problem:

$$\delta = C_0 \sqrt{\nu_l t_g} \tag{4.1}$$

where t_g is the growth time, C_0 a dimensionless constant, and $\nu_l = \mu_l/\rho_l$. Under constant bubble growth rate U_b, we obtain the dimensionless form:

$$\delta^* = C_0 \sqrt{(\mu_l/\rho_l) * (r/U_b)} = C_0 \sqrt{r^*} \tag{4.2}$$

With an initial bubble dimensionless radius $R^*_{b,0}$, and assuming that the contact line is either pinned at its initial position ($r^* = R^*_{b,0}$) or that its outward motion is negligible compared to the macroscopic bubble growth, then the square root model becomes:

$$\delta^* = C_0 \sqrt{r^* - R^*_{b,0}} \tag{4.3}$$

We present in Figure 7 the square root model along with our numerical simulation results, for the range of capillary numbers of interest, $Ca \in [0.001;\ 0.1]$, and for a low contact angle $\theta = 10^\circ$ for which we observe the formation of the microlayer with negligible motion of the contact line compared to the radial extension of the bubble growth. Numerical simulations at higher contact angles were also performed for sake of generality, with contact angles ranging from 10° to 90°. As long as a microlayer forms, higher contact angle conditions yield identical microlayer profiles away from the contact line region, and do not affect the overall volume of liquid trapped underneath the bubble, as shown in the previous section and in Figure 6.

More specifically, we plot the simulated microlayer profiles δ^* as a function of dimensionless radial distance $r^* - R^*_{b,0}$ on the left panels of Figure 7, for three consecutive times, and for capillary numbers spanning the range of interest: Ca=0.001 (a), Ca=0.01 (c) and Ca=0.1 (e). We note that the microlayer continuously grows over time, and that the portion of the thickness profile that has already formed at a given time remains unchanged at later times, with the exception of the contact line region where the dewetting process increases liquid build-up over time at the inner-edge.

The volume of liquid V_{in} associated with the build-up at the inner edge is typically negligible compared to the total volume of liquid V_{tot} trapped under the bubble ($V_{in}/V_{tot} < 0.1\%$), and will not be modeled in the later portion of the paper. This simplification only applies if the contact line's outward motion is negligible compared to the bubble growth, which depends on the physical behavior of the contact line for a given fluid/solid pair and surface condition. In our numerical experiments, and for the contact angle model described earlier, we note in Guion (2017) that the simplification breaks down for very low capillary numbers ($Ca \to 0$) and large contact angles ($\theta \to 90^\circ$), where the velocity of the contact line approaches the bubble growth rate, and no microlayer is left behind.

In Figures 7 (b) (d) (f), we plot the ratio $\delta^*/\sqrt{r^* - R^*_{b,0}}$ as a function of dimensionless radial distance $r^* - R^*_{b,0}$. We note that the ratio is constant in the central region of the microlayer, and that the magnitude of the ratio is close to 0.5 for all the considered capillary numbers. From this observation, we use $C_0 = 0.5$ in the square root model prediction, and compare it with our simulation results in Figures 8, 9 and 10, for various times and all Ca of interests.

Modeling microlayer formation is particularly important to capture two key boiling characteristics: i) the wall heat flux, and ii) the total volume of liquid trapped underneath the bubble that evaporates and that fuels bubble growth up to its departure from the heated surface. The square root model is able to capture both thickness and volume of the microlayer in the central region, which corresponds to the thin part of the microlayer.

We also conclude from Figures 8, 9 and 10 that the square root model does not capture the outer-edge region of the microlayer, and therefore the total volume of liquid trapped underneath the bubble is underestimated. This conclusion suggests the need for specific modeling of the transition from the central (thin) region of near-zero curvature, to the outer-edge (thick) region, of non-zero curvature which is left for future work.

4.4. *Validating numerical results with experimental data and existing models*

Initially in Cooper & Lloyd (1969), experimental data on organic liquids boiling at low pressures provided estimates of C_0, in the range of 0.5 to 1.0, for which experimental data and square root model were found to agree within $\pm 25\%$.

Recent advances in microlayer thickness measurements at different radial locations and short time scales by Yabuki & Nakabeppu (2016) uncovered two regimes based on a modified Bond number $\hat{Bo}$:

$$\hat{Bo} < 13 : \; C_{exp} = 0.13 Bo^{0.38} \tag{4.4}$$

$$\hat{Bo} \geqslant 13 : \; C_{exp} = 0.34 \tag{4.5}$$

with $\hat{Bo} = \rho_l r^2 U / t\sigma$, and C_{exp} the experimental measurement of C_0. Rearranging $\hat{Bo}$ we obtain $\hat{Bo} = \rho_l U^2 t U / \sigma = t^*/Ca$. The transition at $\hat{Bo} = 13$ correspond to physical times $t = \hat{Bo}\ Ca\ t_c$ in the range of $10^{-3}\mu s$ to $10^{-1}\mu s$ for the case of boiling water at $0.101 MPa$ ($Ca \in [0.001;\ 0.1]$, and $t_c \sim 0.1\mu s$). Therefore, only the second regime is relevant to microlayer formation, which occurs over tens of μs, and we note $C_{exp} = 0.34$ the corresponding experimental measurement of C_0 from Yabuki & Nakabeppu (2016), which is of the same order of magnitude as the value of 0.5 we obtain in our numerical simulations.

Lastly, we use experimental measurements of microlayer thickness to validate our numerical results, for the case of water at saturation at $0.101 MPa$ (data courtesy of Prof. Hyungdae Kim). In the experiment, a high-speed video camera was used to measure bubble radius over time, and an IR camera was used to measure the wall temperature distribution underneath the bubble. From the bubble height and width measurements shown in Figure 2, we conclude that the bubble grew hemispherically. An additional high-speed video camera was used to measure microlayer thickness. The measurement error was assessed using a solid convex lens of known curvature: the error in thickness measurement is found to be $\sim 10\%$ for thicknesses greater than $0.5\mu m$, and $\sim 30\%$ otherwise. The earliest bubble growth rate was measured at $t = 20\mu s$, see in Figure 11, and drops dramatically at early times which indicates that the initial bubble

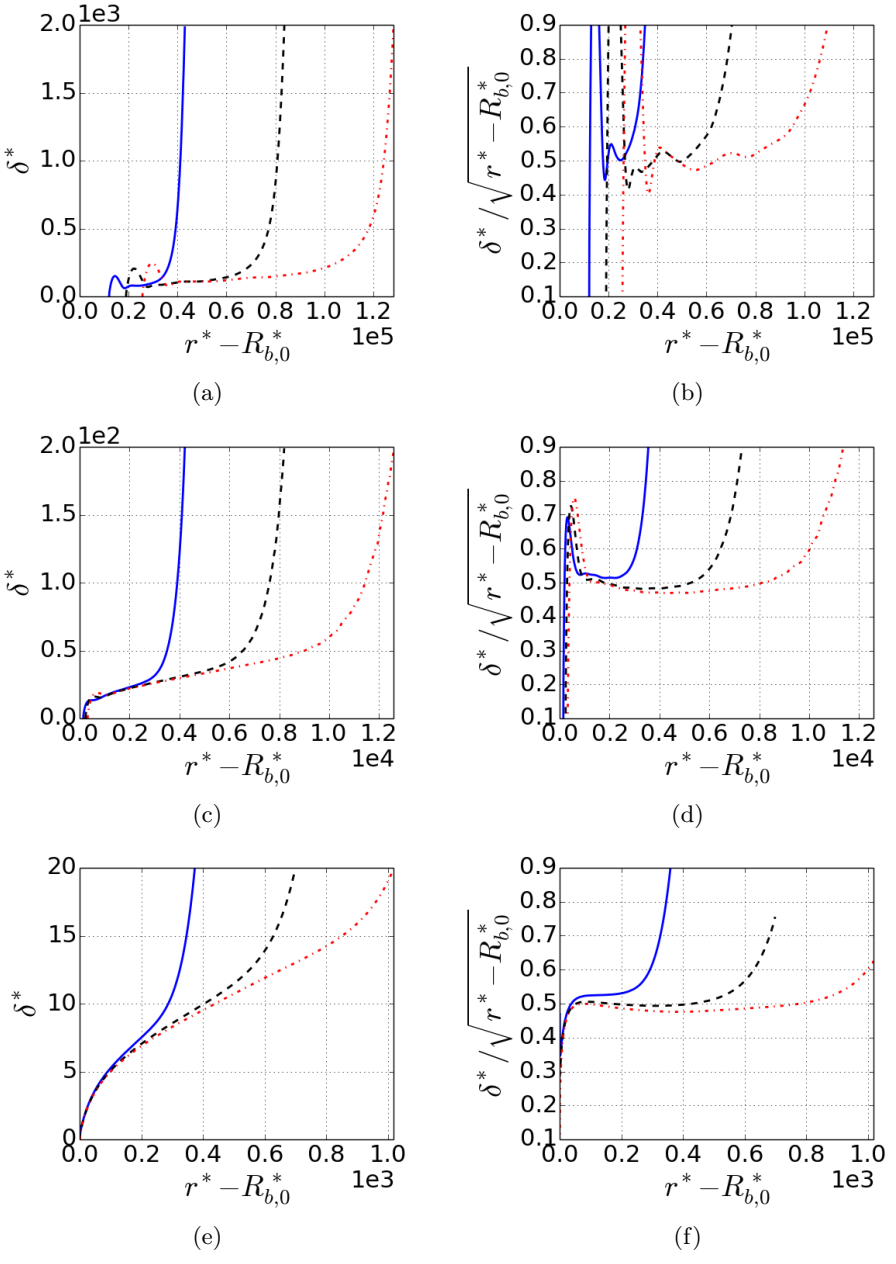

Figure 7: Microlayer dimensionless profiles δ^* plotted in left column: (a), (c), (e), and ratios $\delta^*/\sqrt{r^* - R^*_{b,0}}$ plotted in right column: (b), (d), (f), as a function of dimensionless radial distance $r^* - R^*_{b,0}$, with $R^*_{b,0}$ the initial dimensionless bubble radius. Each row corresponds to a different Ca number: Ca=0.001 in top row (a)(b), Ca=0.01 in middle row (c)(d), Ca=0.1 in bottom row (e)(f). Microscopic contact angle is $\theta = 10°$, and finest mesh size at the wall is $31.25nm$. Same physical times are plotted in all panels: $t = 10\mu s$ (blue solid line), $t = 20\mu s$ (black dashed line), $t = 30\mu s$ (red dot-dashed line). In each row, the following characteristic length and time scales are imposed: ($r_c = 1nm,\ t_c = 1ns$) in top row (a)(b), ($r_c = 10nm,\ t_c = 10ns$) in middle row (c)(d), ($r_c = 0.1\mu m,\ t_c = 0.1\mu s$) in bottom row (e)(f).

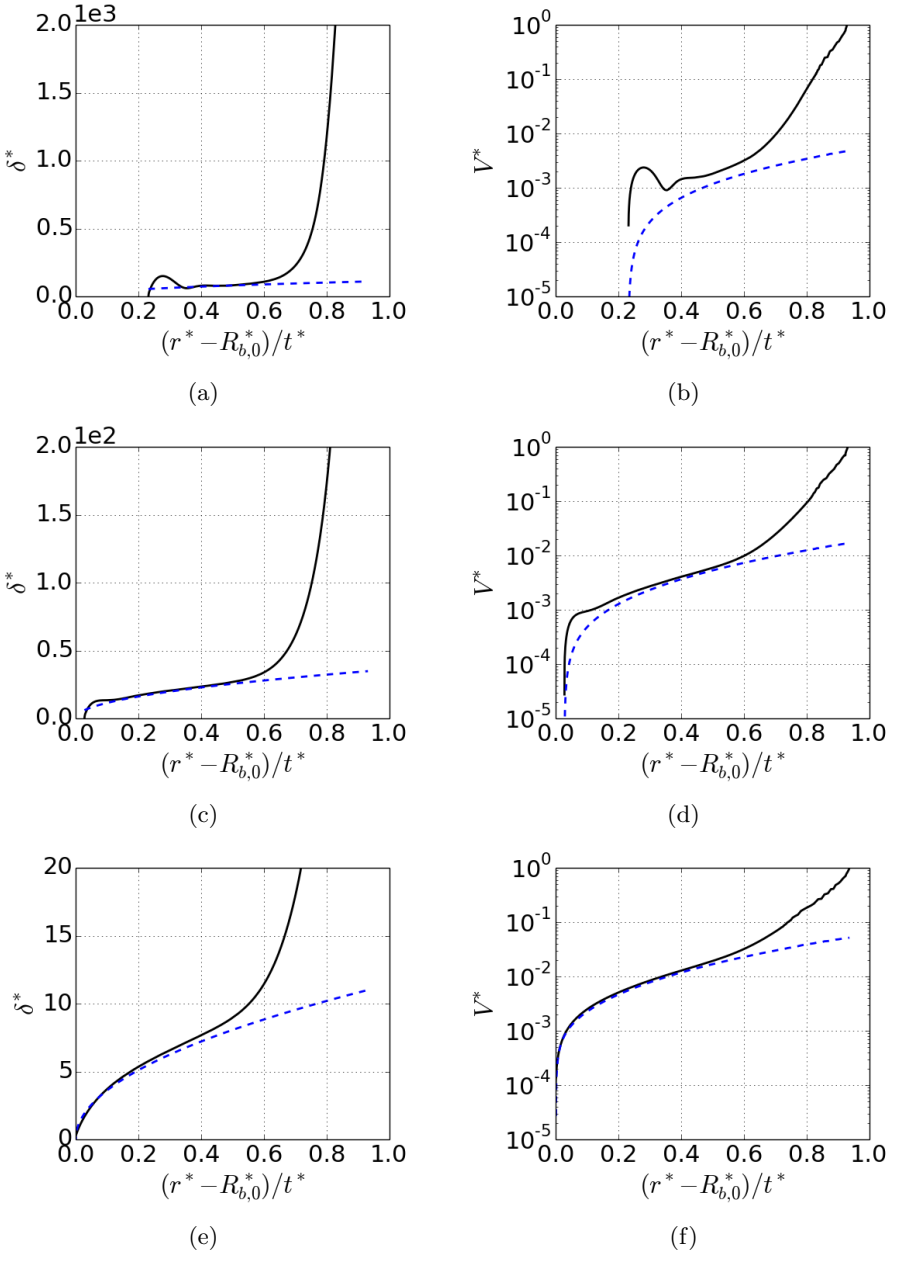

Figure 8: Microlayer dimensionless profiles δ^* (left column) and subsequent volume V^* (right column) with $V^* = V/V_{tot}$, where V_{tot} is the total volume of liquid trapped underneath the bubble), as a function of dimensionless radial extension $(r^* - R^*_{b,0})/t^*$, from simulations (black solid line), and from the square root model: $\delta^* = 0.5\sqrt{r^* - R^*_{b,0}}$ (blue dashed line). Ca=0.001 (top row), Ca=0.01 (middle row), Ca=0.1 (bottom row). Physical time $t = 10\mu s$.

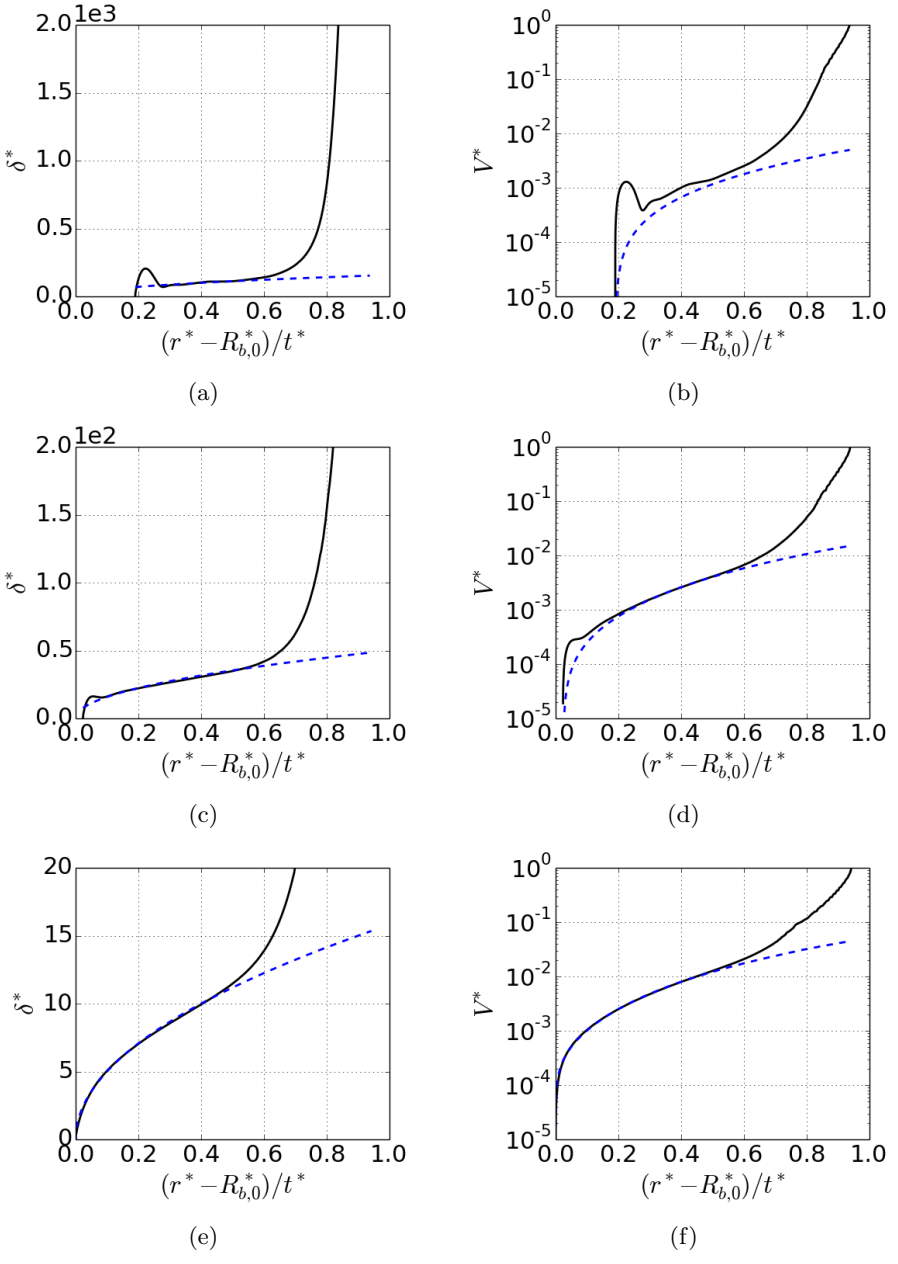

Figure 9: Microlayer dimensionless profiles δ^* (left column) and subsequent volume V^* (right column) with $V^* = V/V_{tot}$, where V_{tot} is the total volume of liquid trapped underneath the bubble), as a function of dimensionless radial extension $(r^* - R^*_{b,0})/t^*$, from simulations (black solid line), and from the square root model: $\delta^* = 0.5\sqrt{r^* - R^*_{b,0}}$ (blue dashed line). Ca=0.001 (top row), Ca=0.01 (middle row), Ca=0.1 (bottom row). Physical time $t = 20\mu s$.

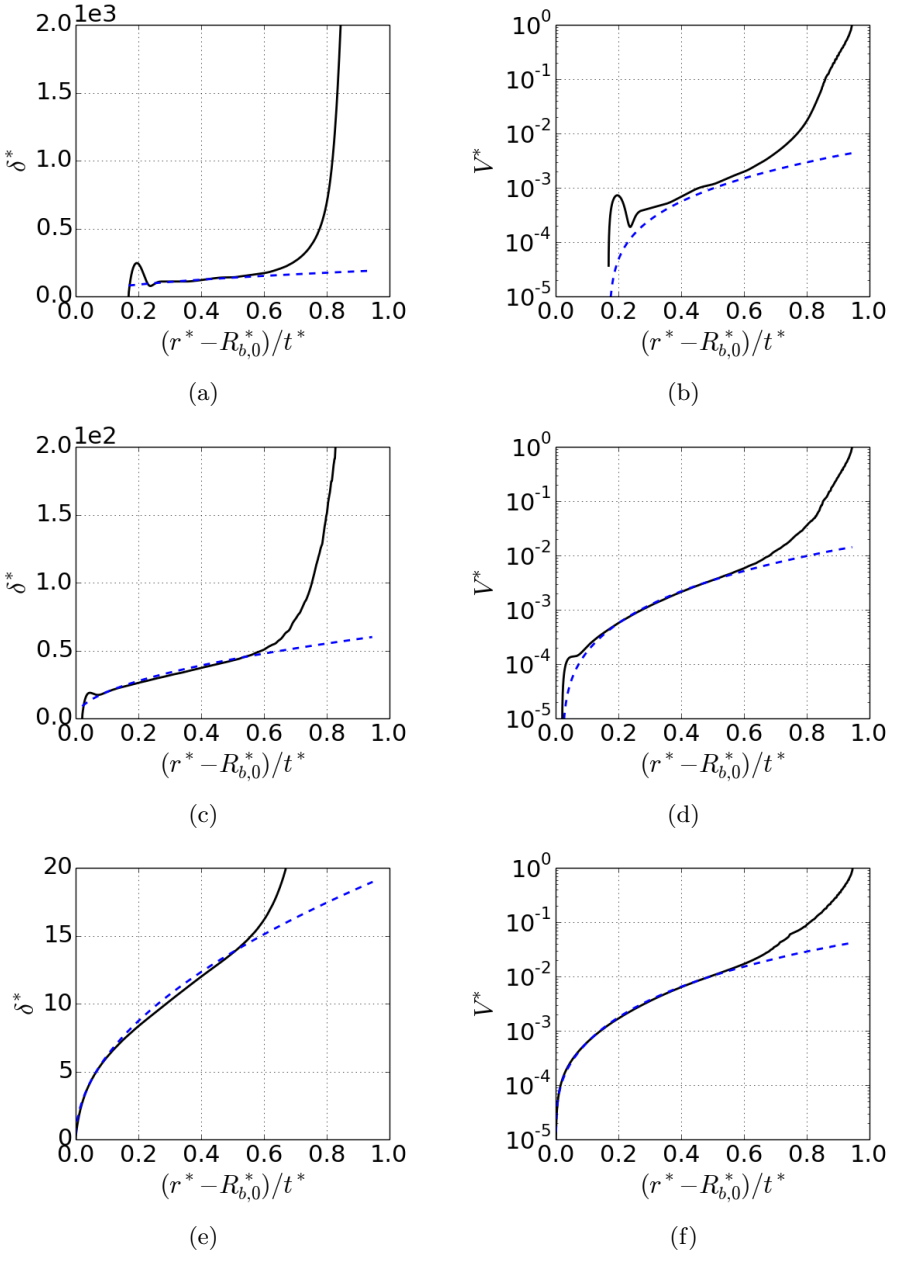

Figure 10: Microlayer dimensionless profiles δ^* (left column) and subsequent volume V^* (right column) with $V^* = V/V_{tot}$, where V_{tot} is the total volume of liquid trapped underneath the bubble), as a function of dimensionless radial extension $(r^* - R^*_{b,0})/t^*$, from simulations (black solid line), and from the square root model: $\delta^* = 0.5\sqrt{r^* - R^*_{b,0}}$ (blue dashed line). Ca=0.001 (top row), Ca=0.01 (middle row), Ca=0.1 (bottom row). Physical time $t = 30\mu s$.

growth rate during the first tens of μs may have been much higher than its first available measured value of $4.2m/s$. We include this uncertainty in initial bubble growth rates in our validation below through a sensitivity study on the initial bubble growth rate: in blue, we assume the bubble growth rate to be constant during the first $20\mu s$, and in red we assume its acceleration to be constant during the first $20\mu s$. We compare our numerical results against experimental results in Figure 11 (b): black squares represent the earliest experimental measurement of the microlayer thickness, which took place at time $t = 410\mu s$; and grey triangles are obtained by deducing the microlayer thickness at $t = 20\mu s$, assuming that the heat transfer within the microlayer is purely by conduction, see Guion *et al.* (2013):

$$\frac{\partial \delta(r,t)}{\partial t} = -\frac{k_l \Delta T_{sat}(r,t)}{\rho_l h_{fg} \delta} \tag{4.6}$$

with k_l the liquid thermal conductivity, ΔT_{sat} the local and time-dependent wall superheat, ρ_l the density of the liquid and h_{fg} the latent heat of vaporization. To simplify the calculation of this estimate, we assume constant wall superheat:

$$\Delta T_{sat}(r,t) = \Delta T_{sat,0}$$

for which a closed form exist:

$$\delta(r,t_0) = \sqrt{\delta(r,t_1)^2 + \frac{2k_l \Delta T_{sat,0}}{\rho_l h_{fg}}(t_1 - t_0)} \tag{4.7}$$

with $t_0 = 20\mu s$, $t_1 = 410\mu s$ and $\Delta T_{sat,0} = 11.7°C$ in our case. Assuming constant wall superheat results in under estimating the thermal coupling with the wall surface, and therefore over estimating the volume of liquid evaporated, in particular in the region of small thickness δ (e.g. low radial distance r). The comparison in Figure 11 between modeled and measured microlayer thicknesses at $t = 20\mu s$ show both qualitative and quantitative agreements.

We also note in Figure 11 a departure from the model in the low thickness region. We expect this discrepancy to be reduced if we no longer assume constant wall superheat, but include the thermal coupling between the microlayer and the heated wall. Such coupling would require to solve for the heat equation in the substrate, while using Eq. 4.6 as a flux boundary condition at the wall surface, as shown in previous work by Guion *et al.* (2013). The initial evaporation of the microlayer would locally reduce the wall superheat and therefore slow down the rate of evaporation of the microlayer. This slow down effect of the microlayer evaporation due to conjugate heat transfer with the solid surface is currently not included in Figure 11, and could explain the over estimated values of the microlayer thickness in the low thickness region at $t = 20\mu s$.

The following properties of water at saturation at $0.101MPa$ were used: $\mu_l = 3.5\ 10^{-4}\ Pa.s$, $\rho_l = 950kg/m^3$. The first measured value of bubble growth rate was $U_b(t \sim 20\mu s) \sim 4.2m/s$.

5. Summary and conclusions

In this work, we used Computational Fluid Dynamics with Interface Tracking Methods to numerically reproduce the hydrodynamics of bubble growth at a wall, and resolve the formation of the liquid microlayer at the wall with high resolution in space and time. We identified the minimum set of dimensionless parameters that controls microlayer formation, and reduced the parameter space for the conditions and fluid of interest, namely water at pressures ranging from $0.101MPa$ (lab conditions) and up to $15.5MPa$

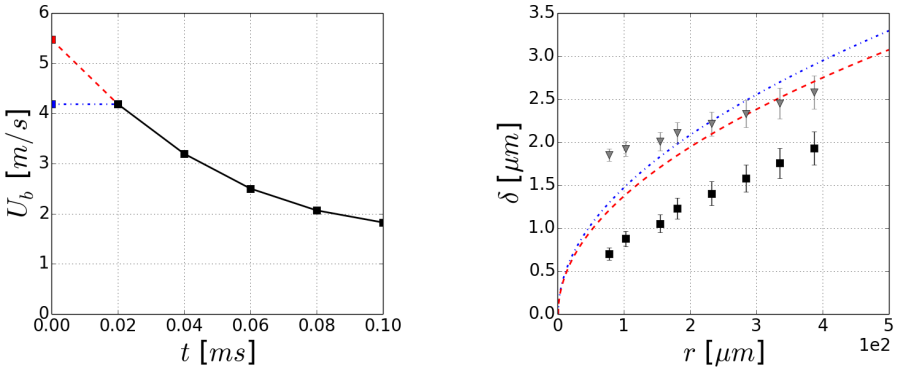

(a) (b)

Figure 11: Measured bubble growth rates (black squares) over time (a), and two assumed initial regimes: constant growth rate (blue dash-dotted line), or constant acceleration (red dashed line). Thickness δ (in μm) measured in lab experiment (black squares) of boiling water at saturation at $0.101MPa$, $0.41ms$ after boiling inception. The deduced microlayer thickness at $t = 20\mu s$ (grey triangles) is obtained assuming that the heat transfer within the microlayer is purely by conduction. The wall temperature at boiling inception is $111.7°C$, and the wall heat flux is $209kW/m^2$ (courtesy of Prof. Hyungdae Kim). Predictions from the square root model are plotted for the two initial profiles of U_b showed in (a). The first measured value of U_b is $U_b(t \sim 20\mu s) \sim 4.2m/s$.

(reactor conditions):

$$\delta^* = f(r^*, t^*, Ca, \theta) \tag{5.1}$$

with δ^* the shape of the extended liquid microlayer, $r_c = \mu_l/(\rho_l U_b)$ and $t_c = r_c/U_b$ the characteristic length and time scales used, respectively. The fluid analyzed in this study is water, however because of the use of dimensionless parameters, the results presented here are broadly applicable to other fluids with dimensionless parameters within the same ranges.

We found that three regions need to be modeled in order to accurately represent the thickness of the microlayer, and the total volume of liquid trapped underneath the bubble:

(i) the inner region: our qualitative results confirm that the dynamics of the moving contact line at the inner edge of the microlayer dictate whether a microlayer forms or not. The proposed methodology can be used to include a physical mobility law in place of the current static microscopic contact angle used, and simulate the liquid build-up at the inner edge for a given fluid/solid pair and surface conditions for which the motion of the contact line is known.

(ii) the central region: our simulation results indicate that the square root model proposed by Cooper & Lloyd (1969) captures the central region of the microlayer accurately in the case of hemishperical bubble growth:

$$\delta^* \approx 0.5\sqrt{r^* - R^*_{b,0}} \tag{5.2}$$

as long as the motion of the contact line is negligible compared to the bubble growth

rate. In addition, we benchmark our results against the earliest microlayer thickness measurements available (courtesy of Prof. Hyungdae Kim), and conclude on both qualitative and quantitative match.

(iii) the outer region: we note that the square root model breaks down at the microlayer outer-edge, where its curvature rapidly increases to meet the non-zero curvature of the bubble cap.

These results clarify the remaining steps needed to build a general model on microlayer formation that resolves the initial and rapid phase of bubble growth in nucleate boiling, called inertia-controlled phase, which lasts a tens of μs in the case of water at atmospheric pressure. The next phase of bubble growth, the thermal diffusion controlled phase, is much slower and lasts tens of milliseconds in the case of water at atmospheric pressure. In practice, the microlayer formation model allows initialization of boiling simulations at the end of the rapid inertia-controlled phase of bubble growth during which the microlayer forms.

Lastly, we conclude that the numerical methods used in this study have proved to be mature enough to investigate microlayer formation and its parameter space of interest, within reasonable simulation time while achieving sufficiently fine spatial and temporal resolution. However, additional experimental data on moving contact lines and microlayer thickness profiles at very short time and length scales relevant to microlayer formation are still needed to continue to benchmark numerical simulations and unlock potential predicting capabilities.

REFERENCES

Afkhami, S, Buongiorno, J, Guion, A, Popinet, S, Scardovelli, R & Zaleski, S 2017 Transition in a numerical model of contact line dynamics and forced dewetting. *arXiv preprint arXiv:1703.07038* .

Afkhami, S & Bussmann, M 2008 Height functions for applying contact angles to 2d vof simulations. *International Journal for Numerical Methods in Fluids* **57** (4), 453–472.

Afkhami, S, Zaleski, S & Bussmann, M 2009 A mesh-dependent model for applying dynamic contact angles to vof simulations. *Journal of Computational Physics* **228** (15), 5370–5389.

Agbaglah, G, Josserand, C & Zaleski, S 2013 Longitudinal instability of a liquid rim. *Physics of Fluids* **25** (2), 022103.

Bankoff, SG 1958 Entrapment of gas in the spreading of a liquid over a rough surface. *AIChE Journal* **4** (1), 24–26.

Bigham, S & Moghaddam, S 2015 Role of bubble growth dynamics on microscale heat transfer events in microchannel flow boiling process. *Applied Physics Letters* **107** (24), 244103.

Brenner, Michael P & Gueyffier, Denis 1999 On the bursting of viscous films. *Physics of Fluids* **11** (3), 737–739.

Buongiorno, J, Cahill, D, Hidrovo, C, Moghaddam, S, Schmidt, A & Shi, L 2014 Micro-and nanoscale measurement methods for phase change heat transfer on planar and structured surfaces. *Nanoscale and Microscale Thermophysical Engineering* **18** (3), 270–287.

Chung, J N, Chen, T & Maroo, S 2011 A review of recent progress on nano/micro scale nucleate boiling fundamentals. *Frontiers in Heat and Mass Transfer* **2** (2).

Churaev, NV 1975 The effect of adsorbed layers on van der waals forces in thin liquid films. *Colloid & Polymer Science* **253** (2), 120–126.

Cooper, MG & Lloyd, AJP 1969 The microlayer in nucleate pool boiling. *International Journal of Heat and Mass Transfer* **12** (8), 895–913.

Dhir, VK 1998 Boiling heat transfer. *Annual Review of Fluid Mechanics* **30** (1), 365–401.

Dhir, VJ 2009 Simulation of boiling: How far have we come! In *Proceedings of 7th ECI International Conference on Boiling Heat Transfer, Florianópolis, Brazil, May*, pp. 3–7.

Foltz, GE & Mesler, RB 1970 The measurement of surface temperatures with platinum films during nucleate boiling of water. *AIChE Journal* **16** (1), 44–48.

Gao, M, Zhang, L, Cheng, P & Quan, X 2013 An investigation of microlayer beneath nucleation bubble by laser interferometric method. *International Journal of Heat and Mass Transfer* **57** (1), 183–189.

Gerardi, C 2009 Investigation of the pool boiling heat transfer enhancement of nano-engineered fluids by means of high-speed infrared thermography. PhD thesis, Massachusetts Institute of Technology.

Gilman, L 2014 Development of a general purpose subgrid wall boiling model from improved physical understanding for use in computational fluid dynamics. PhD thesis, Massachusetts Institute of Technology.

Giustini, G, Jung, S, Kim, H & Walker, SP 2016 Evaporative thermal resistance and its influence on microscopic bubble growth. *International Journal of Heat and Mass Transfer* **101**, 733–741.

Golobic, I, Petkovsek, J, Baselj, M, Papez, A & Kenning, DBR 2009 Experimental determination of transient wall temperature distributions close to growing vapor bubbles. *Heat and mass transfer* **45** (7), 857–866.

Gordillo, L, Agbaglah, G, Duchemin, L & Josserand, C 2011 Asymptotic behavior of a retracting two-dimensional fluid sheet. *Physics of Fluids* **23** (12), 122101.

Guion, A 2017 Modeling and simulation of liquid microlayer formation and evaporation in nucleate boiling using computational fluid dynamics. PhD thesis, Massachusetts Institute of Technology.

Guion, A, Langewisch, D & Buongiorno, J 2013 On the Liquid Microlayer Underneath a Vapor Bubble Growing at a Heated Wall. *International Conference on Multiphase Flow* pp. 1–13.

Hendricks, R & Sharp, R 1964 Initiation of cooling due to bubble growth on a heating surface. *NASA Technical Note D-2290* pp. 1–18.

Hospeti, N B & Mesler, R B 1965 Deposits formed beneath bubbles during nucleate boiling of radioactive calcium sulfate solutions. *AIChE Journal* **11** (4), 662–665.

Jawurek, HH 1969 Simultaneous determination of microlayer geometry and bubble growth in nucleate boiling. *International Journal of Heat and Mass Transfer* **12** (8), 843IN1847–846IN2848.

Jiang, YY, Osada, H, Inagaki, M & Horinouchi, N 2013 Dynamic modeling on bubble growth, detachment and heat transfer for hybrid-scheme computations of nucleate boiling. *International Journal of Heat and Mass Transfer* **56** (1), 640–652.

Judd, RL 1975 Laser interferometric investigation of the microlayer evaporation phenomenon. *Journal of Heat Transfer* p. 89.

Judd, RL & Hwang, KS 1976 A comprehensive model for nucleate pool boiling heat transfer including microlayer evaporation. *ASME J. Heat Transfer* **98** (4), 623–629.

Jung, S & Kim, H 2014 An experimental method to simultaneously measure the dynamics and heat transfer associated with a single bubble during nucleate boiling on a horizontal surface. *International Journal of Heat and Mass Transfer* **73**, 365–375.

Jung, S & Kim, H 2015 An experimental study on heat transfer mechanisms in the microlayer using integrated total reflection, laser interferometry and infrared thermometry technique. *Heat Transfer Engineering* **36** (12), 1002–1012.

Kandlikar, S G 2012 History, advances, and challenges in liquid flow and flow boiling heat transfer in microchannels: a critical review. *Journal of Heat Transfer* **134** (3), 034001.

Kharangate, C R & Mudawar, I 2017 Review of computational studies on boiling and condensation. *International Journal of Heat and Mass Transfer* **108**, 1164–1196.

Kim, Hyungdae & Buongiorno, Jacopo 2011 Detection of liquid–vapor–solid triple contact line in two-phase heat transfer phenomena using high-speed infrared thermometry. *International Journal of Multiphase Flow* **37** (2), 166–172.

Kim, Jungho 2009 Review of nucleate pool boiling bubble heat transfer mechanisms. *International Journal of Multiphase Flow* **35** (12), 1067–1076.

Koffman, LD & Plesset, MS 1983 Experimental study of microlayer formed during vapour bubble growth on the heated solid surface. *Trans ASME J Heat Transf* **105**.

Kunkelmann, Christian & Stephan, Peter 2010 Modification and extension of a standard volume-of-fluid solver for simulating boiling heat transfer. In *Proc. 5th European Conference on Computational Fluid Dynamics ECCOMAS CFD2010, Lisbon, Portugal*.

Kurul, N & Podowski, Mm Z 1990 Multidimensional effects in forced convection subcooled boiling. In *Proceedings of the Ninth International Heat Transfer Conference*, , vol. 2, pp. 19–24. Hemisphere Publishing New York.

Manglik, R M 2006 On the advancements in boiling, two-phase flow heat transfer, and interfacial phenomena. *Journal of Heat Transfer* **128** (12), 1237–1242.

Mikic, BB, Rohsenow, WM & Griffith, P 1970 On bubble growth rates. *International Journal of Heat and Mass Transfer* **13** (4), 657–666.

Moghaddam, S & Kiger, K 2009 Physical mechanisms of heat transfer during single bubble nucleate boiling of fc-72 under saturation conditions-i. experimental investigation. *International Journal of Heat and Mass Transfer* **52** (5), 1284–1294.

Moore, Franklin D & Mesler, Russell B 1961 The measurement of rapid surface temperature fluctuations during nucleate boiling of water. *AIChE Journal* **7** (4), 620–624.

Moriarty, JA & Schwartz, LW 1992 Effective slip in numerical calculations of moving-contact-line problems. *Journal of Engineering Mathematics* **26** (1), 81–86.

Popinet, Stéphane 2009 An accurate adaptive solver for surface-tension-driven interfacial flows. *Journal of Computational Physics* **228** (16), 5838–5866.

Rednikov, A & Colinet, P 2013 Singularity-free description of moving contact lines for volatile liquids. *Physical Review E* **87** (1), 010401.

Sato, Y & Niceno, B 2015 A depletable micro-layer model for nucleate pool boiling. *Journal of Computational Physics* **300**, 20–52.

Savva, N & Bush, J WM 2009 Viscous sheet retraction. *Journal of Fluid Mechanics* **626**, 211–240.

Scardovelli, R & Zaleski, S 1999 Direct numerical simulation of free-surface and interfacial flow. *Annual Review of Fluid Mechanics* **31** (1), 567–603.

Stephan, P & Kern, J 2004 Evaluation of heat and mass transfer phenomena in nucleate boiling. *International Journal of Heat and Fluid Flow* **25** (2), 140–148.

Taylor, GI & Michael, DH 1973 On making holes in a sheet of fluid. *Journal of fluid mechanics* **58** (04), 625–639.

Van Stralen, SJD, Sohal, MS, Cole, R & Sluyter, WM 1975 Bubble growth rates in pure and binary systems: combined effect of relaxation and evaporation microlayers. *International Journal of Heat and Mass Transfer* **18** (3), 453–467.

Warrier, G R & Dhir, V K 2006 Heat transfer and wall heat flux partitioning during subcooled flow nucleate boiling: a review. *Journal of Heat Transfer* **128** (12), 1243–1256.

Weinstein, O & Pismen, LM 2008 Scale dependence of contact line computations. *Mathematical Modelling of Natural Phenomena* **3** (1), 98–107.

Yabuki, Tomohide & Nakabeppu, Osamu 2014 Heat transfer mechanisms in isolated bubble boiling of water observed with mems sensor. *International Journal of Heat and Mass Transfer* **76**, 286–297.

Yabuki, T & Nakabeppu, O 2016 Microlayer formation characteristics in pool isolated bubble boiling of water. *Heat and Mass Transfer* pp. 1–6.

Yeh, LT 1995 Review of heat transfer technologies in electronic equipment. *Transactions of the ASME-P-Journal of Electronic Packaging* **117** (4), 333–339.

Zou, A, Chanana, A, Agrawal, A, Wayner Jr, P C & Maroo, S C 2016*a* Steady state vapor bubble in pool boiling. *Scientific Reports* **6**.

Zou, A, Singh, D P & Maroo, S C 2016*b* Early evaporation of microlayer for boiling heat transfer enhancement. *Langmuir* **32** (42), 10808–10814.